JGR Atmospheres

RESEARCH ARTICLE
10.1029/2018JD029521

Estimate of Turbulent Energy Dissipation Rate From the VHF Radar and Radiosonde Observations in the Antarctic

M. Kohma[1], K. Sato[1], Y. Tomikawa[2], K. Nishimura[2], and T. Sato[3]

[1]Department of Earth and Planetary Science, Graduate School of Science, The University of Tokyo, Tokyo, Japan, [2]National Institute of Polar Research and The Graduate University for Advanced Studies (SOKENDAI), Tokyo, Japan, [3]Department of Communications and Computer Engineering, Kyoto University, Kyoto, Japan

Key Points:
- Two estimates of turbulent kinetic energy dissipation rates based on radar and radiosonde measurements in the Antarctic are given
- Height and seasonal variation of the two estimates have similar features, although the radiosonde-based estimates are 2–5 times larger
- The ratio of the two estimates varies with height, which may reflect overestimation in radiosonde estimation for deep overturning layers

Correspondence to:
M. Kohma,
kohmasa@eps.s.u-tokyo.ac.jp

Citation:
Kohma, M., Sato, K., Tomikawa, Y., Nishimura, K., & Sato, T. (2019). Estimate of turbulent energy dissipation rate from the VHF radar and radiosonde observations in the Antarctic. *Journal of Geophysical Research: Atmospheres*, *124*, 2976–2993. https://doi.org/10.1029/2018JD029521

Received 4 SEP 2018
Accepted 15 FEB 2019
Accepted article online 25 FEB 2019
Published online 18 MAR 2019

Abstract This study estimated the turbulent kinetic energy dissipation rates (TKEDRs) from 1-year observations of the Program of the Antarctic Syowa Mesosphere-Stratosphere-Troposphere/Incoherent Scatter radar (PANSY radar) from October 2015 to September 2016 and compared the results with estimates from radiosonde measurements based on Thorpe's method. The radar-based estimates showed that the TKEDR at Syowa Station was on the order of 10^{-5}–10^{-3} m^2/s^3 in the altitude range of 1.5–19 km. Taking the proportional constant for Thorpe's method (the ratio of the Thorpe scale to Ozmidov scale) as unity, the radiosonde-based measurements show values of TKEDR larger than radar-based estimates by a factor of 2–5. The difference in the TKEDR between radiosonde- and radar-based estimates is larger in the middle and upper troposphere than in the stratosphere. According to previous observational and numerical studies, Thorpe's method tends to overestimate the TKEDR for deep overturning layers. It is confirmed that the depth of the overturning layer is negatively correlated with the difference between radiosonde- and radar-based estimates. The seasonal variation was also examined. An analysis using the distance from the local tropopause level showed that the local maximum in the TKEDR around the tropopause is particularly clear in austral summer. This is likely connected to the seasonality in the gravity wave activity in the Antarctic stratosphere.

1. Introduction

The previous observational studies tried to estimate the turbulent kinetic energy dissipation rate (TKEDR, ε) in the free atmosphere, which is the rate of loss of the TKE due to turbulent dissipation per unit mass (Batchelor, 1953). In the spectral space, the dissipation rate is calculated by integration across the wave number space of the kinetic energy loss rate due to molecular viscosity per unit mass:

$$\varepsilon = \int \nu k^2 E(k) \mathrm{d}k$$

where ν is the kinematic molecular viscosity, k is the wave number, and $E(k)$ is the spectral density of velocity fluctuations. Under Kolmogorov's locality hypothesis, in isotropic, homogeneous turbulence, the ε is equal to the spectral energy flux or the cascade rate within the inertia subrange. The kinetic energy reduction by turbulent dissipation is ultimately converted into internal heating, which can have a significant effect on the heat budget, particularly in the mesosphere and lower thermosphere (e.g., Becker, 2012). The ε is related to the vertical eddy diffusivity (or turbulent diffusivity) K_{zz} under the assumption of equilibrium among energy generation due to the Reynolds stress, energy loss due to buoyancy flux, and molecular dissipation in a stably stratified flow (Fukao et al., 1994):

$$K_{zz} = \gamma \frac{\varepsilon}{N^2}$$

where γ is the mixing coefficient and N is the buoyancy frequency. The mixing efficiency is considered to depend on the turbulence generation and the degree of supersaturation of the waves (McIntyre, 1989). High-resolution estimates from radar indicated that the range of γ is from 0.06 to 0.3 in the upper troposphere and lower stratosphere (Dole et al., 2001). A recent observational study suggests that the mixing coefficient is around 0.16–0.2 in both the atmosphere and ocean (Kantha & Luce, 2018).

Previous studies examining the mean stratospheric age of air (AoA, Dietmüller et al., 2017; Ploeger et al., 2015) showed that on the order of 10% of the mean AoA is attributable to subgrid-scale mixing (diffusion), although its impact is minor compared to the residual mean circulation and mixing by resolved-scale motions. Recently, Dietmüller et al. (2018) quantified the impact of mixing on the stratospheric mean AoA using chemistry-climate model intercomparison (CCMVal-2 and CCMI-1) and pointed out that differences in subgrid-scale mixing likely explained the spread in the AoA between the models.

Estimates of turbulent parameters in the free atmosphere have been obtained from very high frequency (VHF) clear-air Doppler radar measurements based on the received power and width of the Doppler spectrum with a high height-time resolution. Two methods for estimating ε are commonly used: the spectral method and the power method (Hocking, 2011; Wilson, 2004). The former has been widely used since the 1980s (Hocking, 1983; Sato & Woodman, 1982) and is based on the fact that the spectral width of backscattering echoes is related to the turbulent velocity variance. The latter relates the radar reflectivity with the structure constant of the refractive index. For the power method, an absolute calibration of the radar and the fraction of the radar volume filled with turbulence are necessary, while the spectral method does not require this. Delage et al. (1997) compared ε obtained from these two methods and showed good agreement for turbulent layers thinner than 600 m. The estimates from VHF radars of the turbulent parameters including ε and eddy diffusivity were reviewed by Hocking (1999), Wilson (2004), and Hocking (2011).

Several previous studies obtained the temporal variation and climatology of ε and turbulent diffusivity using the spectral width method in the middle latitudes (Hocking, 1988; Nastrom & Eaton, 1997, 2005; Sato et al., 1995), the tropics (Rao et al., 2001) and the northern high latitudes (Li et al., 2016). Nastrom and Eaton (1997, 2005) pointed out that the frequency distribution of ε at a given height is approximately lognormal. Nastrom and Eaton (1997) showed vertical profiles of ε as a function of both distance above the surface and distance relative to the tropopause. It was revealed that ε at the White Sand Missile Range (32°N, 106°W) is maximized at the lowest observed altitude and minimized below the tropopause. Li et al. (2016) examined 1-year observations by the Middle Atmosphere Alomar Radar System radar at Andoya, Norway (69.03°N, 16.04°E) and showed that ε generally increases with height in the troposphere and through the lower stratosphere.

Instruments with a high time-vertical resolution have been used for estimating the turbulent parameters. Alisse and Sidi (2000), Luce et al. (2002), and Gavrilov et al. (2005) performed balloon-borne radiosonde observations with a vertical resolution of 10 cm and calculated the Thorpe length scale, L_T, that is indicative of the local overturning scale (Thorpe, 1977). This Thorpe analysis is characterized by rearrangement of the measured density or potential temperature profile into a monotonic profile. The Thorpe displacement is defined as the vertical displacement of a parcel from the measured to sorted profiles, and the Thorpe scale of an overturning layer is calculated as the root-mean-square of the Thorpe displacement for the layer. The Thorpe analysis was originally developed for estimation of the oceanic turbulent parameters using measurements of density profiles from conductivity-temperature-depth casts. Based on accumulated oceanic turbulence observations, the Thorpe scale is thought to be related to the Ozmidov scale, L_O, by a proportional constant in a stably stratified flow (e.g., Dillon, 1982):

$$L_O = cL_T \tag{1}$$

Since the Ozmidov scale is defined as $(\varepsilon/N^3)^{0.5}$, the Thorpe scale can be used for estimation of the turbulent kinetic energy dissipation rates (TKEDRs):

$$\varepsilon_T = c^2 L_T^2 N^3 \tag{2}$$

Alisse and Sidi (2000) showed that turbulent layers have significantly larger L_T (~9 m) than calm layers (~1 m). In contrast to previous studies based on measurements with a vertical resolution of tens of centimeters, Clayson and Kantha (2008) applied the Thorpe analysis to raw pressure-temperature-humidity (PTU) data from operational radiosonde observations with a moderately high vertical resolution (~several meters) to derive the turbulent parameters. Wilson et al. (2010) proposed a procedure for the selection of statistically significant overturn structures from temperature profiles with instrumental noises. Wilson et al. (2011) showed that the turbulence patches on the largest scales could be detected by the 10-m-resolution radiosonde measurements. Following Clayson and Kantha (2008) and Wilson et al. (2010, 2011), Thorpe

analysis-based estimates using radiosonde observations have been reported by several studies. For example, Bellenger et al. (2017) showed the climatology of eddy diffusivity and overturning size in the troposphere over the Indian Ocean based on about 3,500 radiosonde observations. Because of recent improvements in the resolution of radiosonde measurements, which typically have a vertical resolution of ~5 m (Love & Geller, 2012), the Thorpe analysis can now be applied to the present global network of radiosonde measurements. Applying the Thorpe analysis to a global network of radiosonde measurements may provide information on the spatiotemporal variability of the turbulent parameters in the troposphere and stratosphere (Kantha & Hocking, 2011), which is not currently known, although several studies tried to derive structure functions over a wide spatial coverage using rawinsondes (e.g., Frehlich & Sharman, 2010).

In order to diagnose the energy dissipation rates using the Thorpe scale, we have to determine the proportional coefficient c in equation (1), which is the ratio of the Thorpe scale to the Ozmidov scale. It is known that the ratio, however, has a large uncertainty (0.25–4), which leads to the uncertainty of ε with 2 orders of magnitude. Schneider et al. (2015) derived vertical profiles of ε with a balloon-borne anemometer at a sampling rate of 8 kHz and compared them with estimates from the Thorpe analysis. They showed that the proportional coefficient had quite a broad range, whereas the most probable value of $(L_O/L_T)^2$ is 0.1. Moreover, previous observational and modeling studies reported the time dependence of the ratio (e.g., Mater et al., 2015; Smyth et al., 2001). Smyth et al. (2001) used direct numerical simulation (DNS) to show that the ratio increases monotonically with time as the Kelvin-Helmholtz billow collapses. The results of DNS obtained by Fritts et al. (2016) indicate that L_T, L_O, and their ratio are highly variable, depending not only on the stage of the turbulence but also on the source of the turbulence, including Kelvin-Helmholtz instability and gravity wave breaking.

Recently, Scotti (2015) discussed whether the Thorpe scale is equivalent to the displacement length scale for turbulent flow using an energetic framework formulated by Scotti and White (2014). Decomposing the available potential energy (APE) and other quantities into the mean and turbulent components, they showed that the Thorpe scale generally includes not only the turbulent displacement length scale but also a contribution from the mean APE. They also performed DNS experiments to examine two extreme turbulent regimes. One is the turbulent flow driven by the kinetic energy of the mean flow, which does not include any APE of the mean flow in the initial conditions (namely, shear-driven turbulence). The other is the convective-driven turbulence, which is driven by the APE of the mean flow. Scotti (2015) indicated that the Thorpe method gives good estimates of the dissipation in the shear-driven turbulence, while for the convective-driven case, the Thorpe-analysis-based estimates are much larger than the true dissipation. Mater et al. (2015) also found a significant positive bias in the Thorpe scale-based dissipation for the oceanic turbulence in the Luzon Strait, where deep overturn is often observed.

Several previous studies compared radar-based estimates to the Thorpe analysis using radiosonde observations. Kantha and Hocking (2011) and Li et al. (2016) compared the ε estimated from the Thorpe analysis with those from the Harrow VHF radar (42.04°N, 82.89°W) and the Middle Atmosphere Alomar Radar System radar, respectively. Note that both studies used unity as the proportional constant in equation (1). They reported reasonable agreement between the statistics, including the median values and frequency distribution, obtained by the radiosondes and the VHF radars, although a one-to-one correspondence is not always observed. Both of the previous studies, however, made use of measurements from nine radiosondes at most. Considering the highly intermittent nature of the turbulence, a larger number of simultaneous observations from radiosondes and radars are desirable for verifying the validity of the Thorpe analysis in the free atmosphere.

In this study, the TKEDRs are estimated from the 1-year observations of the Program of the Antarctic Syowa Mesosphere-Stratosphere-Troposphere/Incoherent Scatter radar (PANSY radar; Sato et al., 2014) at Syowa Station (69.00°S, 39.35°E) and compared with estimates from operational radiosonde observations. Radiosonde measurements were routinely performed twice a day at Syowa Station. The present study utilized hundreds of radiosonde profiles simultaneously with the radar measurements. The altitude dependence and seasonality of ε are also investigated. This is the first report on the turbulent parameters in the troposphere and lower stratosphere in the Antarctic to our knowledge. It should be noted that the seasonal variation of the tropopause structure including the tropopause inversion layer (TIL) over the Antarctic is quite different compared to other latitudes (Tomikawa et al., 2009).

Table 1
Parameters of the PANSY Radar

Title	Value
Location	Syowa Station, Antarctic (69.00°S, 39.35°E)
Operating central frequency	47.0 MHz
Interpulse period	320 μs
Peak power output	520 kW
Coherent integration	64 times
Incoherent integration	7 times
Nyquist velocity	±15.6 m/s
Spectral resolution	0.244 m/s
Range resolution	150 m
Number of beams	5 (vertical +10° oblique to north, south, east, and west)

This study is organized as follows. A description of the data used is given in section 2. The methods for radar-based and radiosonde-based estimation are summarized in section 3. Annual mean vertical profiles and the seasonal variation of ε rates are given in section 4. A comparison with previous estimates at other latitudes based on a vertical coordinate defined as the distance relative to the tropopause is presented in section 5, along with a discussion on the discrepancy between the two kinds of estimates. The summary and concluding remarks are given in section 6.

2. Data

2.1. PANSY Radar at Syowa Station

The PANSY radar is the first Mesosphere-Stratosphere-Troposphere/Incoherent Scatter radar in the Antarctic region. Continuous observations have been made by the PANSY radar through a partial system since 30 April 2012. After two campaign measurements with a full system (16–24 March 2015 and 5 April–16 May 2015; e.g., Minamihara et al., 2016), the radar has been in continuous full-system operation since late September 2015. We used 1-year observation data from the radar for October 2015 to September 2016, during which time the radar performed observations almost continuously. Because the radar was designed to be energy efficient, the data were obtained with almost no interruption over the whole year despite the limited power availability in the Antarctic. The time resolution of the data was ~90 s, although the observation time intervals were ~200 s because of interleaving observations for the mesosphere. The analyses were made in the height range from 1.5 to 24 km. The vertical resolution was 150 m along the beam direction. We used measurements by four oblique (northward, eastward, southward, and westward) beams with a zenith angle of 10° because specular reflection rather than isotropic scattering due to isotropic turbulence affects the spectrum for the vertical beam (e.g., Fukao et al., 1994; Tsuda et al., 1986). Kantha et al. (2017) suggest that the advantage of using the vertical beam for estimating velocity variance is that there is no need for shear broadening correction. Nevertheless, we used the oblique beams because the analyzed height region includes tropopause region, which is characterized by the sharp gradient of static stability causing the specular reflection (e.g., Birner, 2006). Note that the aspect sensitivity of the radar is quite small outside of the tropopause region (e.g., Sato et al., 2014), and thus, the applicability of measurements by the vertical beam for estimating turbulent parameters will be investigated in future studies.

Note that the two-way beam pattern was not circular due to the irregular antenna distribution (Sato et al., 2014). We thus extracted the turbulent velocity variance considering the antenna distribution, as will be described later. Details of the PANSY radar are documented in Sato et al. (2014). The radar parameters are shown in Table 1.

2.2. Radiosondes

We used measurements by Meisei RS-06G soundings, which were performed routinely at Syowa Station. The radiosondes are launched approximately 500 m west of the PANSY radar twice a day (around 23:30 UT and 11:30 UT). The time resolution of the data is 1 s and the ascending rate of the balloons is around 6 m/s.

In the process for creating standard PTU outputs for the Meisei RS-06G radiosonde, filtering and smoothing are applied to temperature profiles above 300 hPa in order to reduce erroneous spikes during daytime observations (Meisei Electronics, personal communication, 2017; Shimizu & Hasebe, 2010). This is also the case for standard products from other commonly used radiosondes (e.g., Dirksen et al., 2014). The filter for the radiosonde is designed to trace the lower envelope of temperature. Although the filtered profiles are appropriate for operational purposes, they are not suited for detecting overturning layers accompanied by turbulence. For that reason, we reprocessed the raw binary data into temperature data without smoothing and filtering (hereinafter referred to as the reprocessed raw temperature). Previous studies applying the Thorpe analysis method to radiosonde measurements also used the raw PTU data from other radiosondes.

Before applying the Thorpe analysis, the quality of the reprocessed raw temperature data was investigated, since spikes due to instrumental error including the warm wake of the balloon can contaminate temperature

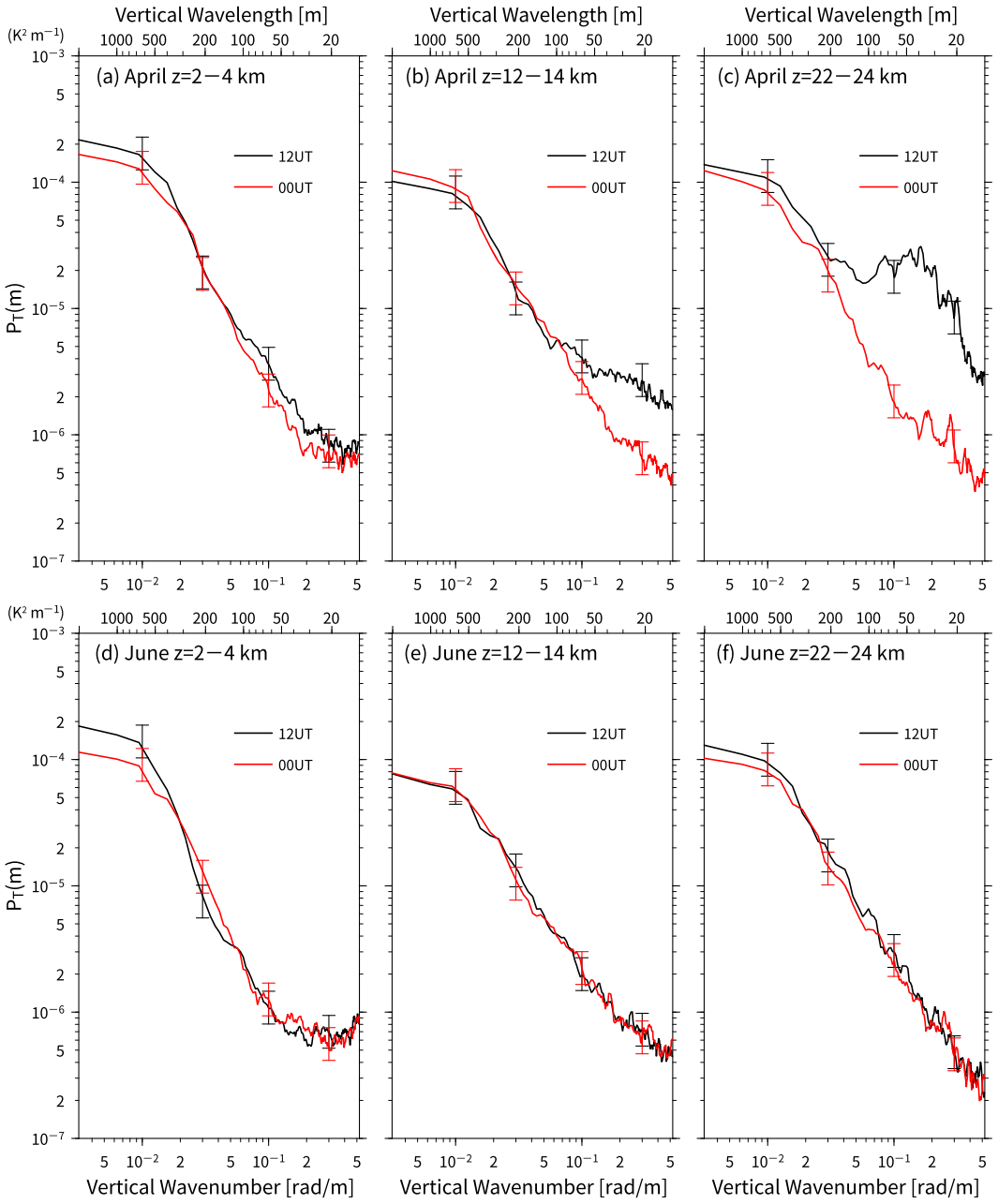

Figure 1. (a–c) Vertical wave number power spectra of temperature fluctuations in April 2016 for altitude ranges of (a) 2–4, (b) 12–14, and (c) 22–24 km. Red (black) curves indicate measurements for 00 UT (12 UT). Error bars show the 99% confidence intervals of the spectra. (d–f) Same as Figures 1a–1c but for June 2016 in (d) 2–4, (e) 12–14, and (f) 22–24 km.

profiles. Figure 1 shows the vertical wave number power spectra for temperature in April 2016 for three altitude ranges, namely, 2–4, 12–14, and 22–24 km. The power spectra for profiles at 11:30 and 23:30 UT were calculated separately. Note that sunset is from 12:30 to 14:30 UT and sunrise is from 4:00 to 6:00 UT in April at Syowa Station. The temperature spectra at 11:30 UT resemble those at 23:30 UT for vertical wavelengths of 200–1,000 m for all three altitude ranges. For vertical wavelengths shorter than 100 m, however, the spectra at 11:30 UT are significantly larger than those at 23:30 UT. The difference in the spectral density becomes larger at higher altitudes. For example, the spectral density at altitudes of 22–24 km (Figure 1c) at 11:30 UT is 1 order of magnitude greater at a vertical wavelength of 60 m than that at 23:30 UT. Figures 1d–1f are the same as Figures 1a–1c but for June 2016. Note that Syowa Station is in

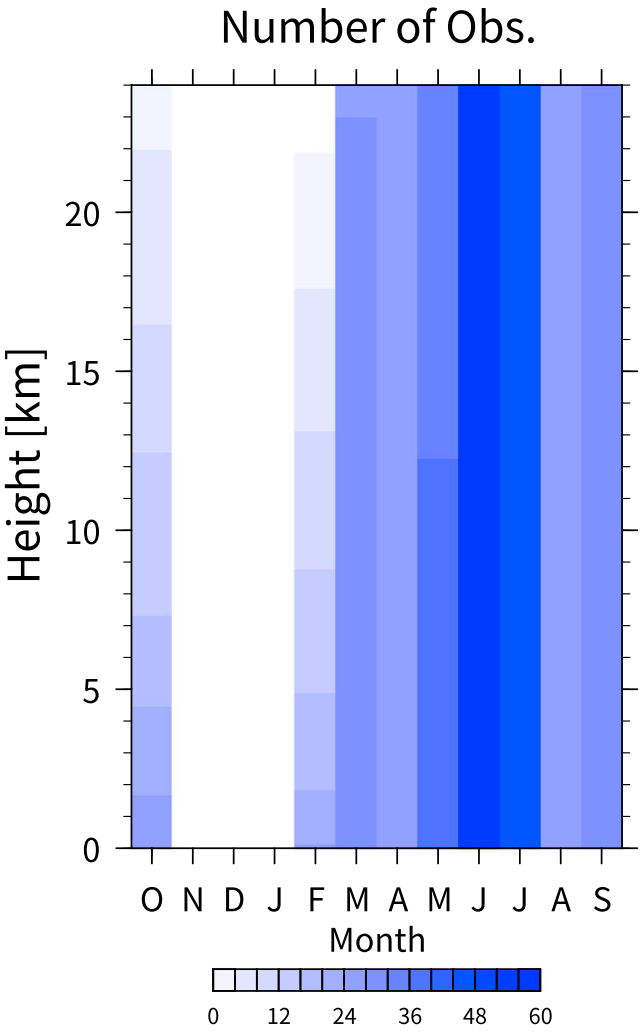

Figure 2. Number of radiosonde profiles that the present study used for the Thorpe analysis as a function of height and month. No data from November through January were used.

the polar night throughout June. It is found that the difference in the spectra between 11:30 and 23:30 UT is insignificant for the displayed wavelength range and height ranges.

These results strongly indicate that the daytime radiosonde temperature observations contain large instrumental errors for wavelengths shorter than ~100 m, which covers most of the range of overturn sizes that have been reported in previous studies (e.g., Bellenger et al., 2017; Kantha & Hocking, 2011; Wilson et al., 2011). Several previous studies (e.g., Luce et al., 2014; Wilson et al., 2018) pointed out the large error in the raw PTU data for the daytime observations that affects the quality of the Thorpe analysis. The cause of the daytime instrumental noise was previously discussed in Shimizu and Hasebe (2010), Dirksen et al. (2014), and Kizu et al. (2018) and is outside the scope of the present study. Thus, the present analyses used the reprocessed raw temperature data for the nighttime only. Sunset and sunrise times at Syowa Station for each day and height were obtained from the website of the National Astronomical Observatory of Japan (http://eco.mtk.nao.ac.jp/cgi-bin/koyomi/koyomix_en.cgi). Taking the duration of the radiosonde ascent from the launching location during measurement into consideration, the measurements in the period from 2 hr after sunset to 2 hr before sunrise were analyzed. Figure 2 shows the monthly variations in the number of available nighttime profiles as a function of altitude. More than 40 profiles are available in May through July. No data are available in November through January.

2.3. Miscellaneous Data

The present study used the Japanese 55-year Reanalysis (Kobayashi et al., 2015) to calculate the height of the dynamical tropopause (Hoskins et al., 1985). In the present study, the dynamical tropopause height is defined as the height with a potential vorticity (PV) of -2×10^{-6} K·m^2·kg^{-1}·s^{-1}. The present study used data on a 1.25° × 1.25° regular latitude-longitude grid, and the PV values at Syowa Station were obtained by linear interpolation.

3. Methods for Estimating ε

3.1. Estimation of ε From Spectral Width of Radar Echo

In the present study, the turbulent parameters were derived from the spectral widths (Hocking, 1983; Sato & Woodman, 1982). The radar Doppler velocity spectra have a finite spectral width associated with eddies of spatial scales from half of the radar wavelength, λ (~3 m), to the sampled volume thickness (150 m). Other nonturbulent processes, however, also contribute to the spectral broadening, that is, beam-, shear-, and time-broadening effects (Fukao et al., 2014). Thus, in order to extract the contribution of turbulence, σ_{turb}, we have to subtract other broadening effects from the observed spectral width, σ_{obs}, in Hz, namely,

$$\sigma^2_{\mathrm{turb}} = \sigma^2_{\mathrm{obs}} - \sigma^2_{\mathrm{beam}} - \sigma^2_{\mathrm{shear}} - \sigma^2_{\mathrm{time}}$$

where σ_{beam}, σ_{shear}, and σ_{time} represent beam, shear, and time broadening, respectively. The use of a simple formula for subtraction of the beam broadening for a symmetric antenna pattern (Hocking, 1985) is questionable with regard to the PANSY radar, which has an irregular antenna pattern, as mentioned before. Taking the antenna distribution and wind speed direction into consideration, we subtracted the beam-broadening component with a deconvolution operation for the measured spectra. The spectral width is estimated using a Gaussian fitting from the spectra from which the beam-broadening component is subtracted. The broadening due to vertical shear of the horizontal winds, u_z, was estimated as $|u_z|\Delta r \sin\vartheta/2$, where ϑ and Δr are the zenith angle of the main beam and the range of the gate length, respectively (Fukao et al., 2014). This study neglected the time-broadening component, which is normally small compared to other

broadening components (Nastrom & Eaton, 1997). The velocity variance v'^2 relates to σ^2_{turb} through the relation $v'^2 = \sigma^2_{turb}(\lambda/2)^2/(2\ln 2)$.

The velocity variance due to turbulence in a stably stratified flow is linked to the TKEDRs as follows (Hocking, 1983; Weinstock, 1981):

$$\varepsilon \approx c_R v'^2 N_S \tag{3}$$

where c_R was set to 0.45 in the present study, which was derived empirically (Hocking, 1999). Previous studies typically use a value of 0.45 to 0.5 for c_R for the radar estimation (e.g., Hocking, 1999; Wilson, 2004). Note that several studies pointed out that the velocity variance measured by the radar is related with the transverse one-dimensional spectrum function for the direction radial from the radar (Dehghan & Hocking, 2011; Hocking, 1999). Hocking et al. (2016) proposed 0.5 ± 0.25 as the appropriate value range of c_R, which indicates the uncertainty of 50% in radar estimates. The buoyancy frequency, N_S, was calculated as $g d\ln\theta_s/dz$ from the radiosonde observations, where $\theta_s(z)$ is the monotonically sorted dry potential temperature profile.

Another relation between ε and radar spectral width was derived by Labitt (1979) and White et al. (1999). Hocking (1996) showed that the formulation by Labitt (1979) should be applied when the largest cross-volume length of the radar scattering volume is less than one half of the buoyancy scale. Because the range resolution is 150 m and the most of the overturning layers have depth less than 300 m and Thorpe scale less than 150 m in the altitude range of 4–20 km (see also section 5.2), the present study uses equation (3) for estimating the ε.

The data for 11:00–13:00 and 23:00–01:00 UT were used in the present study since the radiosondes were launched at around 11:30 and 23:30 UT. The present study used about 25,000 radar profiles in 2016, and the monthly results were based on at least 1,800 observations. The median values of ε were averaged over the four oblique beams. Note that the calculation of median values uses samples having positive and negative ε values. The difference in the median ε between with and without negative values is quite small (<3%), and we confirmed that this does not essentially affect the following results. The estimated ε from the radar observations is hereinafter denoted ε_R.

3.2. Estimation of ε From Radiosonde Observations

Detection and selection algorithms for overturning layers from radiosonde observations were made following Wilson et al. (2010, 2011). First, the data with irregular intervals were resampled to have regular vertical intervals. A sampling interval of 6 m was chosen in the present study since the ascent rate was typically 6 m/s. The measured pressure was smoothed to a monotonically decreasing profile using a least squares cubic spline fit. Wilson et al. (2011) proposed a simple estimation for the instrumental noise variance in temperature, σ^2_T, from the radiosonde profiles. The temperature profiles are divided into segments at a fixed interval (200 m is typically used). The variance is calculated from the first differences of the detrended temperature profile in each segment, which corresponds to twice the noise variance ($2\sigma^2_T$). However, this estimated noise inherently includes not only instrumental noises but also turbulent fluctuations and curvature of the background temperature profile. In the present study, the noise fluctuation was estimated as the first mode of the intrinsic mode functions from the ensemble empirical mode decomposition (Huang & Wu, 2008). The noise variance is calculated as the square of the fluctuations averaged over a vertical interval of 200 m. Note that the estimated noise level was typically 70% of that from the method by Wilson et al. (2010). The noise variance in the potential temperature, σ_θ, was calculated as $\sigma_T(1{,}000\ \mathrm{hPa}/p)^{2/7}$, where p is the pressure in hPa.

Wilson et al. (2010) suggested that the optimal width of smoothing and undersampling should be determined such that the bulk trend-to-noise ratio is larger than one. The width of undersampling and smoothing was set to two in the present study, which results in a bulk trend-to-noise ratio greater than two for all profiles. The corresponding vertical resolution of the temperature profiles was 12 m. In order to include the effect of latent heat release due to the condensation process, the potential temperature profiles were reconstructed by replacing the potential temperature with the moist-conservative potential temperature in the cloudy sections (Wilson et al., 2013).

The obtained potential temperature profiles were sorted to be monotonically increasing. Thorpe displacement is defined as the vertical displacement from the position of the air parcel in the measured profile to that of the same parcel in the sorted profile. The Thorpe scale is the root-mean-square value of the Thorpe displacement in the respective overturning layers.

The selection procedure proposed by Wilson et al. (2011, 2010) was applied to each overturning layer. Such a procedure is necessary to avoid introducing errors into the artificial overturning layers due to instrumental noise, which was estimated as σ_θ. The overturning layers with a potential temperature variation exceeding the 99th percentile confidence level were considered to be significant (Wilson et al., 2010). This selection procedure rejected about 60% of the detected overturning layers. The percentage of the rejected overturns is comparable to those in the previous studies (e.g., 85% in Bellenger et al., 2017; one third to two thirds in Wilson et al., 2014).

Using the empirical proportional relation between the Thorpe (L_T) and Ozmidov scales (L_O), the energy dissipation rates for radiosonde measurements, ε_T, is calculated following equation (2). We used the bulk buoyancy frequency for N when calculating ε_T because it gives a bulk gradient that is relatively insensitive to the boundaries for the overturning layer (Smyth et al., 2001). The squared bulk buoyancy frequency N_b^2 is defined as $g\theta_{rms}/(\theta_s L_T)$, where θ_{rms} is the root-mean-square of the difference between the measured and sorted values at a given height. The bulk buoyancy frequency is obtained by equating the Thorpe scales with Ellison scale ($\theta_{rms}/\overline{\theta}_z$, where $\overline{\theta}_z$ is a vertical gradient of background potential temperature; Smyth et al., 2001; Wilson et al., 2014). Note that the bulk buoyancy frequency is significantly different from N_S when the sorted potential temperature profiles depart from the linear relation. The proportional coefficient c was set to unity in the present study, which was used in comparisons between radar-based and radiosonde-based estimates in the previous studies (Kantha & Hocking, 2011; Li et al., 2016).

4. Results

4.1. Case Study: 7 June 2016

Figure 3a shows vertical profiles of ε_R (red curve) and ε_T (bar chart) at 12:00 UT on 7 June 2016. The vertical shear of the horizontal wind ($|\partial \boldsymbol{u}/\partial z|$), the buoyancy frequency (N_s), and the gradient Richardson number from the radiosonde measurements smoothed with a low-pass filter having a cutoff length of 600 m are also shown in Figures 3b and 3c. The ε_R for the height regions of 2.9–3.6 km and 7.0–7.5 km was not obtained due to the low radar echo power. The large buoyancy frequency change around 7 km corresponds to the tropopause level. The overall variation of the radiosonde estimates accords well with that of the radar-based estimates. For example, large values (10^{-4}–10^{-3} m^2/s^3) below altitudes of 4 km and above altitudes of 7 km are observed in both estimates. Low value of Richardson number and strong vertical shear in the altitudes of 2.5–3.5 km correspond to a large ε. A closer look, however, shows that the difference amounted to 1 order of magnitude. Note that because the number of overturning layers is small in the stratosphere, a one-to-one comparison between the two estimates at each level is difficult there. In addition, the radiosonde does not necessarily measure the same volume as the radar since the radiosonde drifts away from the radar. In this case, the horizontal distance between the radiosonde and radar at an altitude of 18 km is about 60 km.

Previous studies suggested that a one-to-one correspondence between the radar-based and radiosonde-based estimates is difficult due to the high degree of intermittency and the spatial variability of turbulence in the free atmosphere (Kantha & Hocking, 2011; Li et al., 2016). Thus, many previous studies focused on the statistics of the two estimates although several studies described case studies of turbulent layers from concurrent observations by a radar and radiosondes (e.g., Wilson et al., 2014). The present study also performed a statistical comparison between the radar-based and radiosonde-based estimates in the following section.

4.2. Comparison Between Radar-Based and Radiosonde-Based Estimates

Before comparing the radiosonde-based estimates with the radar-based ones, the difference in the vertical resolution between both estimates should be considered because ε_T is obtained for each overturning layer with a finite depth (Figure 3a). In the following analyses, statistics for the radiosonde-based estimates weighted with respect to the depth of the overturning layer are shown. Furthermore, we assumed that the horizontal distance between the radar and radiosondes had little impact on the statistics, although the radiosondes did not always measure the same volume as the radar.

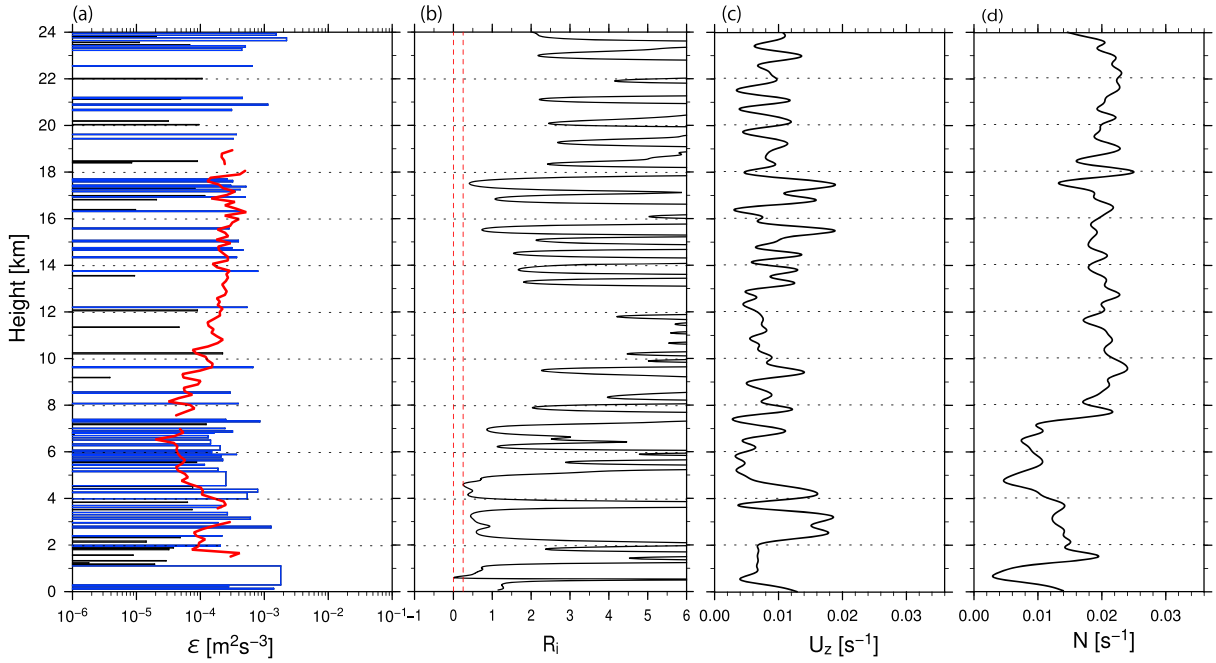

Figure 3. Vertical profiles of (a) estimated ε_T (bar chart) and ε_R (red curve), (b) gradient Richardson number, (c) vertical shear of horizontal wind, and (d) buoyancy frequency at 12:00UT on 7 June 2016. Statistically significant ε_T is indicated with blue lines. Dotted horizontal lines are drawn at an interval of 2 km. The red broken vertical lines in Figure 3b indicate the values of 0 and 0.25.

A normalized histogram of ε_R is shown in Figure 4a at the altitudes below 8 km, which corresponds approximately to the annual mean tropopause height at Syowa Station. The distribution of ε_R is approximately log-normal, and its median value is 2.4×10^{-4} m^2/s^3. Most ε_R values are on the order of 10^{-5}–10^{-3} m^2/s^3. Figure 4c shows ε in the altitude range of 8–19 km, above which the availability of the radar-based estimates is less than 10%. The distribution shows a slightly left heavy-tail feature, which was also reported in the northern high latitudes (Li et al., 2016). Compared to the altitudes below 8 km, ε_R had a slightly larger median value of 3.0×10^{-4} m^2/s^3.

For the radiosonde estimates (Figures 4b and 4d), the median value is 3.6×10^{-4} m^2/s^3 below 8 km and 4.4×10^{-4} m^2/s^3 in 8–19 km. The median values of ε_T for both altitude ranges are larger than those of ε_R. The range of ε_T is approximately 5×10^{-5} to 10^{-2} m^2/s^3. The cutoff of the left tail of the ε_T distribution is likely due to the limited vertical resolution of the radiosonde measurements (Wilson et al., 2011). The asymmetric distribution of ε_T implies that the mode of the distributions may provide the reasonable estimate of ε rather than the median. The modes are 2.8×10^{-4} m^2/s^3 below 8 km and 4.4×10^{-4} m^2/s^3 in 8–19 km. Nevertheless, the median ε is used in the present study for comparison with the ε estimates in the previous studies (e.g., Kantha & Hocking, 2011; Li et al., 2016).

Since the radiosonde-based estimates were applicable to the nighttime data only, the statistics for ε_T in Figure 4 are based on measurements in February through October. For comparison between the two estimates in the same period, we made a normalized histogram of the ε_R in February through October. It is shown that the median value is slightly larger (2.5×10^{-4} m^2/s^3 below 8 km and 3.2×10^{-4} m^2/s^3 in 8–19 km) and the distribution shape is similar (not shown).

4.3. Height Dependence in ε

As seen in Figure 4, ε tends to be large above 8 km compared to altitudes of 1.5–8 km. In order to assess the height dependence of ε in more detail, the radar-based and radiosonde-based ε as a function of height are shown in Figure 5a. The median ε_R (red) falls between 9×10^{-5} and 2×10^{-4} m^2/s^3 at all altitudes. This median range is comparable to that in the northern high latitudes (Li et al., 2016), while it is 1 order of magnitude less than the estimates from the radar in the northern middle latitudes (Nastrom & Eaton, 1997). The local

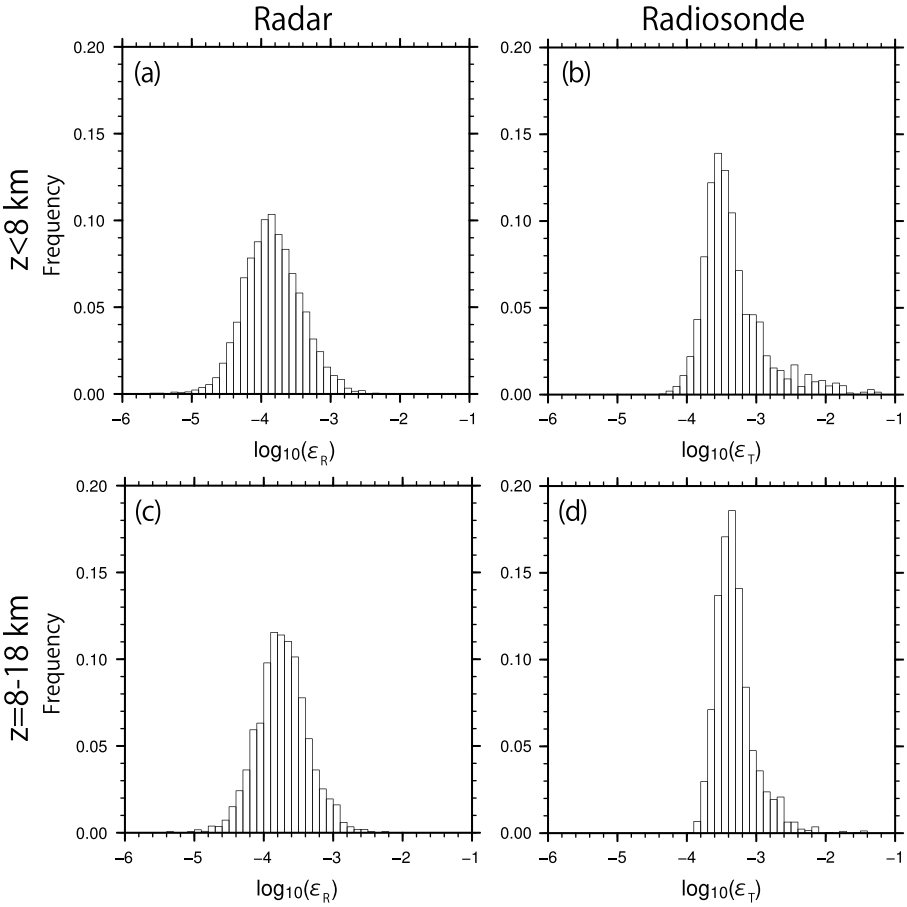

Figure 4. Normalized histograms of ε estimated from (a) radar and (b) radiosondes in the altitude below 8 km. (c, d) The same as Figures 4a and 4b but for altitudes of 8 to 19 km.

maximum of the median ε_R is found at the lowest and highest observed altitudes, and the minimum is found around 6.5 km. The height variation of the median ε_R in 10–19 km is quite small. The ε_R variation seen in Figure 5 is similar to that reported by Li et al. (2016).

The median range of ε_T (blue) is from 3.1×10^{-4} to 1.5×10^{-3} m^2/s^3. The maxima are found at the lowest altitudes, around 10 km, and the highest altitudes. The overall height variations of the median ε_T and ε_R exhibit clear similarities, although ε_T is always larger than ε_R by a factor of 2–5. Note that the difference between the two estimates over all altitudes is within the uncertainty range of the proportional coefficient that relates the Ozmidov scale to the Thorpe scale (Clayson & Kantha, 2008).

It is interesting that the ratio of ε_R to ε_T (i.e., the difference between the red and blue curves in Figure 5a) is large in altitudes of 1.5–9 km compared to over 11 km. Although the coefficient c in equation (1) is set to 1 so far, the optimal (average) value of c is examined in the rest of the present section. Figure 5b shows the square root of the ratio between the median values of ε_R and $L_T^2 N^3$ as a function of height. Figure 5b indicates the value c at a specific altitude that one must multiply $L_T^2 N^3$ in order to have $\varepsilon_R = \varepsilon_T$ according to equation (2) under the assumption that the radar-based estimates provide the reference dissipation rates. The minimum (~ 0.4) is found at the lowest observed altitude, and the proportional coefficient increases to 0.8 at an altitude of 19 km.

The altitudinal dependence of the coefficient has not been pointed out in previous studies using radiosondes and radars, which is likely due to the small number of radiosonde measurements available for comparison (nine at most). For example, Kantha and Hocking (2011) determined the optimal value for L_O/L_T as unity by comparing the vertically integrated histograms of the radiosonde-based and radar-based estimates. The DNS

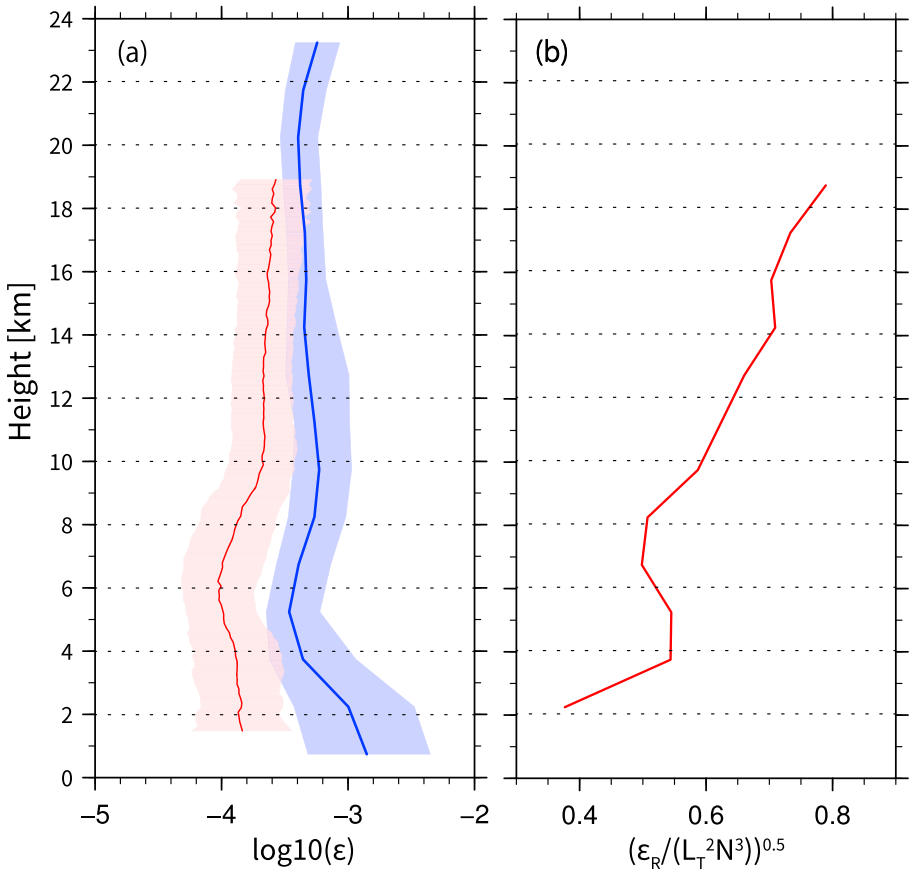

Figure 5. (a) Vertical profiles of median values of logarithms of ε_R (red curve) and $L_T^2N^3$ (blue curve). The red (blue) shaded region indicates the range from the 25th to 75th percentiles for ε_R (ε_T). The vertical bin sizes for ε_R and $L_T^2N^3$ are 150 m and 1.5 km, respectively. (b) Vertical profiles of the square root of the ratio of the median value of $L_T^2N^3$ to that of ε_R. Dotted horizontal lines are drawn at an interval of 2 km.

results and a recent observational study showed that L_O/L_T depends on the event type of the turbulence and its evolution (e.g., Schneider et al., 2015; Scotti, 2015). This point will be discussed in more detail later.

4.4. Seasonal Variation in ε

Next, the seasonality of ε was examined. Note that the seasonal variation mentioned below is based on 1-year measurements in October 2015 through September 2016, and thus, it may not express the climatological features of ε in the Antarctic. An estimate based on multiyear measurements will be shown in future studies.

Figure 6a shows the logarithm of the median ε_R as a function of month and height. Stars indicate the mean dynamical tropopause where PV = -2×10^{-6} K·m^2·kg^{-1}·s^{-1}. Note that the height range for the ε_R is shown only where the availability of the estimates was greater than 10%. As observed in Figure 5, the overall ε_R in the stratosphere is larger than in the troposphere. It is also shown that, above an altitude of 11 km, the ε_R increases in March through April and has a broad maximum in August through November. In January through April, the vertical profiles show a local maximum slightly above the tropopause (9–10 km). The seasonal variation in the troposphere is unclear, although weak broad minima are observed in November through January. At the lowest altitudes, the local maxima are found throughout the analysis period.

For comparison, the squared buoyancy frequency and vertical shear of the horizontal wind from the radiosonde data are shown in Figures 7a and 7b. Both quantities were calculated from the profiles smoothed with a low-pass filter having a cutoff length of 500 m. Typical values of the squared buoyancy frequency are 1.4 and 4×10^{-4} s^{-2} in the troposphere and stratosphere, respectively. For the austral winter and spring, an increase in the buoyancy frequency with height is observed in the lower stratosphere. The buoyancy

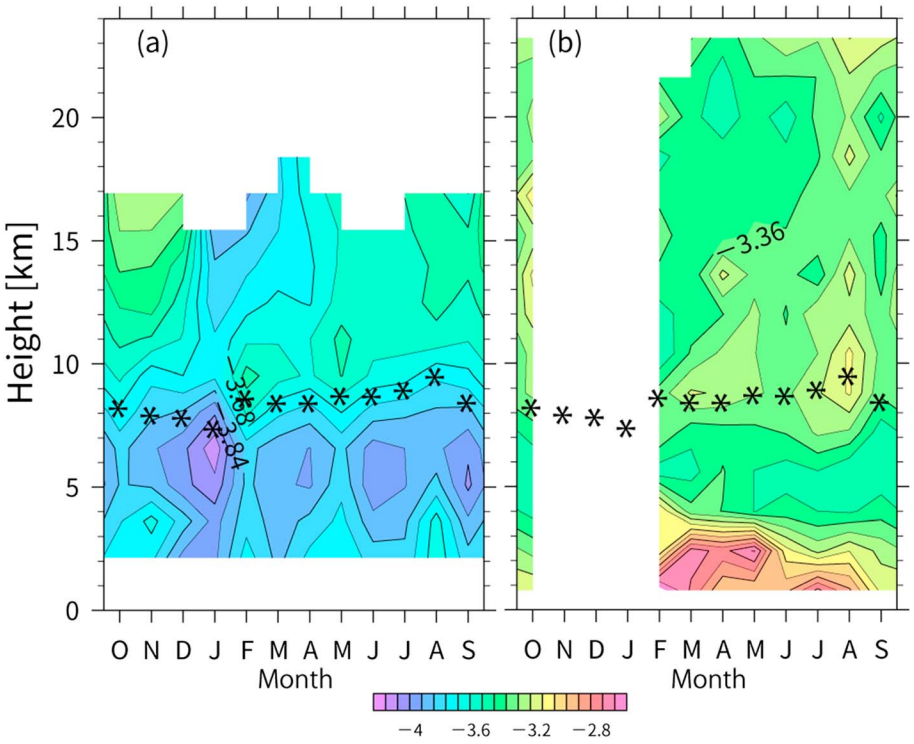

Figure 6. Monthly median values of logarithms of (a) ε_R and (b) ε_T as functions of height. The vertical bin size is 1.5 km. The stars indicate the monthly averaged tropopause heights determined from the local PV at Syowa Station. PV = potential vorticity.

frequency has a local maximum just above the tropopause in the austral summer through fall, which corresponds to the TIL (e.g., Randel et al., 2007), whereas a sustained inversion above the tropopause was not observed clearly in June through October. The local maximum 1–2 km above the ground in the austral winter and spring is likely associated with radiative cooling at the ground. These features are consistent with the climatology at Syowa Station obtained by Tomikawa et al. (2009), who examined comprehensively the seasonal variation in the buoyancy frequency and ozone around the tropopause level at Syowa Station.

The vertical shear of the horizontal wind has three peaks in the analyzed altitude range: the lowest altitudes, around 1 km above the tropopause, and the highest altitudes. The two maxima in the stratosphere are particularly clear in the austral fall through spring. The vertical shear in the middle and upper troposphere is small compared to that around the ground and above the tropopause. The frequency of gradient Richardson number less than 1.0 is also shown in Figure 7c. The strong vertical shear indicates a lowering Richardson number at the same altitudes. The height and temporal variation of the strong vertical shear and low Richardson number shows good accordance with the large ε_R. The seasonal evolution of the vertical shear above 11 km, which shows large values in the austral late winter and early winter, bears some similarity to that of ε_R.

In addition to the background vertical shear, buoyancy frequency, and gradient Richardson number, the gravity wave activity was examined to explore the cause of the seasonal variation of ε in the lower stratosphere. Figures 7c and 7d show the variations of the potential energy (PE) and kinetic energy (KE) of gravity waves per unit mass, respectively. The gravity-wave components of the temperature and horizontal wind were extracted following Yoshiki et al. (2004): Four-day running mean profiles are regarded as the background field. The gravity-wave components were defined as the deviations from the background field whose vertical wavelengths were between 1 and 8 km. In the height region of 11–15 km, weak but broad maxima of the gravity wave PE and KE are observed. The seasonal variation of gravity wave PE and KE in 11–15 km largely accords with that of ε_R at the same altitudes.

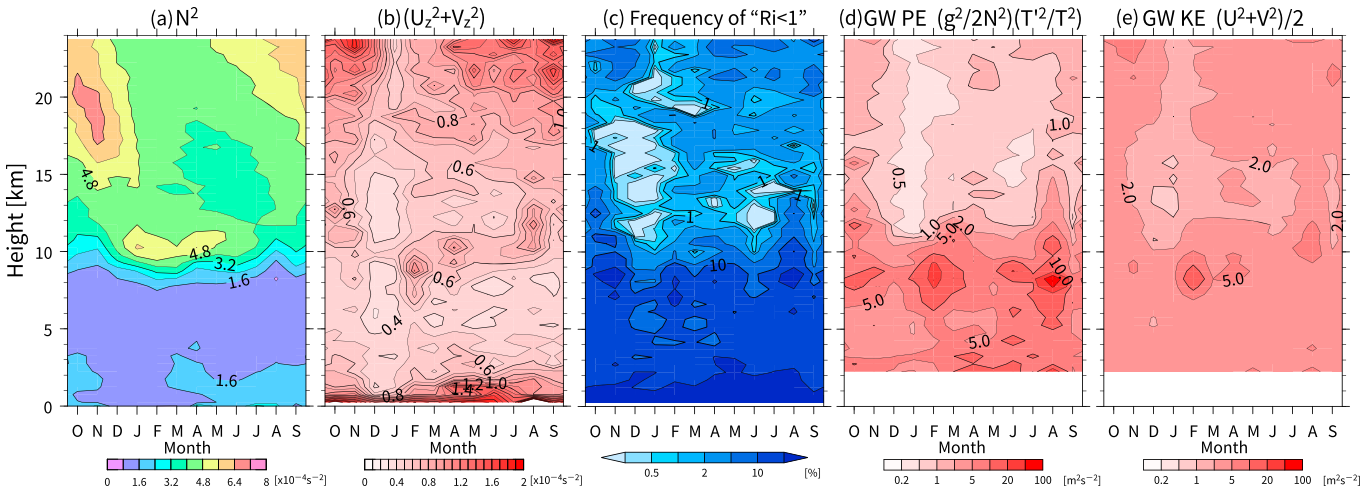

Figure 7. Same as Figure 6 but for monthly mean (a) squared buoyancy frequency, (b) squared vertical shear of horizontal wind, (c) frequency of gradient Richardson number less than 1.0, and (d) potential energy and (e) kinetic energy of gravity waves per unit mass.

Figure 6b shows the radiosonde-based estimates, which only included measurements in February through October. In 11–15 km, the seasonal variation of ε_T shows a broad range of maxima in August through October, and lower values in February and March, which is consistent with the features of ε_R. This indicates that radiosonde-based estimates capture the seasonal variation in the radar-based ε in the lower stratosphere (Figure 6a).

The radiosonde-based estimates are also available above 15 km. In this altitude range, the ε_T is large in late winter and early spring. In spring, warming occurs earlier at higher altitudes and the region of high buoyancy frequency propagates downward. The gravity wave energy shows clear seasonal variation having a maximum in spring during the downward propagation of high buoyancy frequency (Figure 7a), which was reported in Yoshiki and Sato (2000) and Yoshiki et al. (2004). The seasonal evolution of ε_T in 18–25 km bears a resemblance to that of the gravity wave PE and KE at the same altitudes.

5. Discussion

5.1. Profiles Relative to the Tropopause Height

Previous studies showed a drastic change in the turbulent parameters across the tropopause. Nastrom and Eaton (1997) used the distance from the tropopause as the vertical coordinate and found an abrupt transition of ε in the northern midlatitudes during all seasons. Following them, vertical profiles of the median ε_R in December through February (DJF, black) and June through August (JJA, red) are shown as a function of the distance from the dynamical tropopause height (Figure 8a). Both profiles show large ε_R in the stratosphere and small ε_R in the troposphere, and the values in the stratosphere were larger by a factor of 2.5 at most. At a height of 1.6–3.5 km below the tropopause, ε_R for DJF and JJA have similar values.

Figures 8b and 8c show the turbulent velocity variance (v'^2) from the radar spectral width and buoyancy frequency in the same vertical coordinate. The velocity variance in DJF had its maximum about 1 km above the tropopause and decreased with height in the stratosphere. In JJA, a slight increase in the velocity variance with height is found over the whole range. The buoyancy frequency in DJF is higher than in JJA except for around the tropopause. The maximum buoyancy frequency associated with the TIL was pronounced in DJF, whereas it disappeared in JJA (Figure 7a).

The seasonal variation of the ε_R is quite small 1.6–3.5 km below the tropopause. Considering the linear dependence of ε_R on v'^2N (equation (3)), this is because the buoyancy frequency has an opposite-sign seasonal variation compared to that of the velocity variance. Nastrom and Eaton (1997) first pointed out the opposite-sign seasonal variations of the velocity variance and buoyancy frequency for the northern

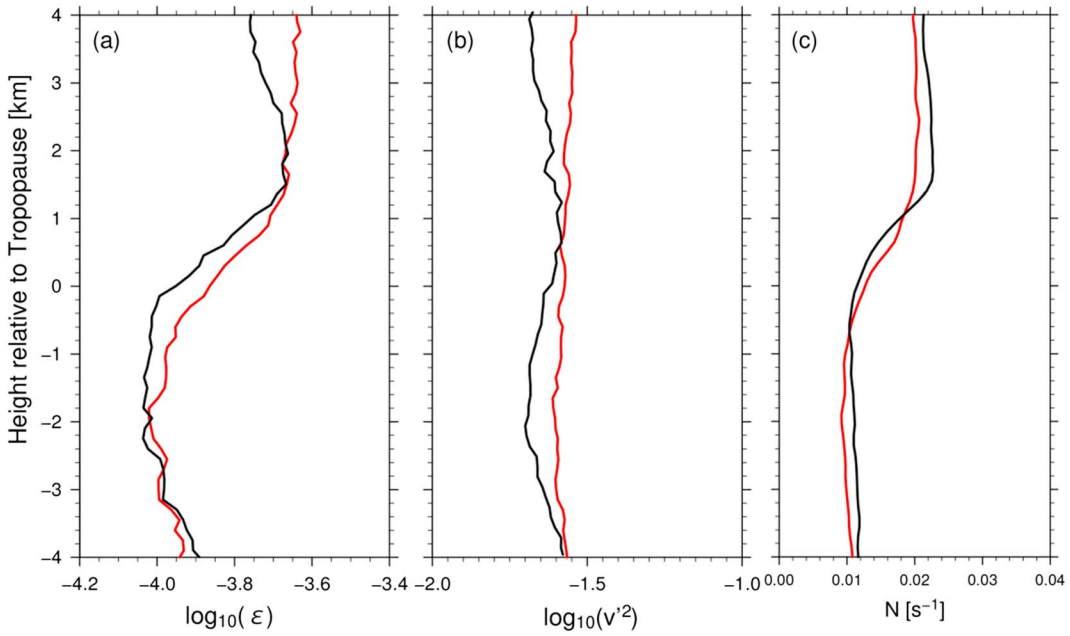

Figure 8. Vertical profiles of median values of (a) logarithm of ε_R, (b) turbulent velocity variance, and (c) buoyancy frequency as a function of distance from the dynamical tropopause. Black (red) curves indicate profiles for DJF (JJA).

midlatitudes, and thereby the resulting small seasonal variation of ε. Nastrom and Eaton (2005) pointed out a similar relation between the buoyancy frequency and velocity variance in the northern low latitudes.

The seasonal variation of ε_R is pronounced at a height of 3–4 km above the tropopause (i.e., stratosphere), which is in good accordance with that of the velocity variance contrast between DJF and JJA. It is also shown that the velocity variance has the opposite sign for the seasonal variation compared to that of the buoyancy frequency.

Nastrom and Eaton (1997, 2005) showed the prominent maxima of ε just above the tropopause in winter and spring for the northern latitudes. In contrast to Nastrom and Eaton (1997, 2005), the maxima of the ε_R and velocity variance are observed in DJF (i.e., austral summer) at Syowa Station. Considering seasonal variation of the gravity wave activity (Figures 7c–7d), the latitudinal difference in the turbulent parameters is likely attributable to gravity wave activity in the Antarctic stratosphere (Figures 7c and 7d).

5.2. Comparison With Previous Studies Based on Oceanic Microstructure Profilers and DNS

The comparison between the radar-based and radiosonde-based estimates showed that the ratio of the two estimates varied with height (Figure 5). This fact means that the proportional coefficient relating the Thorpe scale and Ozmidov scale, $c = L_T/L_O$, is not constant in the vertical direction. It should be noted that both estimations are based on the stratified fluid (equations (2) and (3)). Thus, the estimates within the atmospheric boundary layer (up to 3 km at most) should be interpreted with caution. Nevertheless, the decrease of the difference in ε with height is observed in the free atmosphere.

Recent direct comparison of L_T and L_O for oceanic turbulence implies that for flows dominated by deep overturning associated with oceanic tides and steep topography, the Thorpe analysis results in a large positive bias in ε (Mater et al., 2015), which is consistent with theoretical and DNS results by Scotti (2015). In order to examine the relation between depth of overturning and the proportional coefficient, the vertical profile of L_T and depth of overturning layers, D, are shown in Figure 9. The local maxima of the median L_T and D are found at the lowest and at an altitude of 8 km. In the altitude range from 8 km to 19 km, the median L_T and D decrease with height. Both the height variations are well negatively correlated with that of the difference between radar and radiosonde estimates. This suggests that the height variation of the difference between the two estimates may be attributable to overestimation of Thorpe's method associated with deep overturning events.

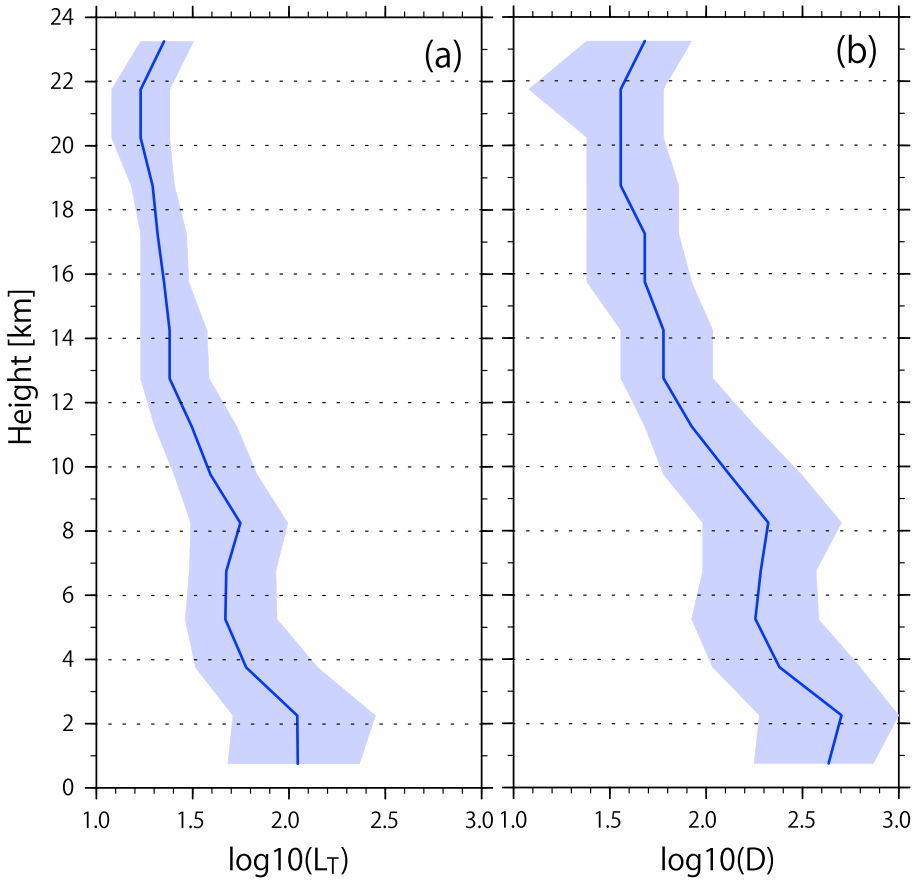

Figure 9. Same as Figure 5a but for L_T and overturning depth D from radiosonde measurements.

6. Summary and Concluding Remarks

Using 1-year observations from the PANSY radar and radiosondes at Syowa Station in the Antarctic, we examined the seasonal variation of turbulent parameters, particularly the TKEDRs (ε). This study gives the first estimates of the turbulent parameters in the Antarctic free atmosphere. A large number of observations provide an opportunity to explore the seasonal and altitudinal variation of ε. The present study used unity as the ratio of the Thorpe scale to Ozmidov scale. The results are summarized as follows:

1. The radar-based ε has a lognormal distribution and a range from 10^{-5} to 10^{-2} m^2/s^3 for altitudes of 1.5–19 km. The median values were 2.4×10^{-4} m^2/s^3 at 1.5–8 km and 3.0×10^{-4} m^2/s^3 at 8–19 km.
2. The median values of the radiosonde-based ε are 3.6×10^{-4} m^2/s^3 in 1.5–8 km and 4.3×10^{-4} m^2/s^3 in 8–19 km. The lower bound of the radiosonde-based ε is 5×10^{-5} m^2/s^3, which is noticeably larger than the radar-based estimates.
3. The radar-based and radiosonde-based ε show similar height dependence, although the radiosonde-based ε is 2–5 times larger: local maxima in the lowest altitudes, minima in the middle troposphere, and approximately constant in the lower stratosphere.
4. The ratio between the radiosonde-based and radar-based ε also has height dependence (Figure 5b). Specifically, the ratio is greater at altitudes below 8 km than above an altitude of 11 km. According to the direct comparison between Ozmidov scale and Thorpe scale in the previous study, the height variation of the ratio might represent the vertical variation of the depth of the overturning layers.
5. Seasonal variation in the radar-based ε shows a broad maximum in August through October and low values in November through January in the lower stratosphere. The variation on a seasonal time scale is unclear in the troposphere.
6. From an analysis using the distance from the local tropopause height, it was shown that the local maximum in ε around the tropopause is particularly clear in DJF (austral summer) while ε increases

monotonically across the tropopause in JJA (austral winter). This is likely connected to the seasonality in the gravity wave activity in the Antarctic.

The present statistical analysis based on about 370 radiosonde measurements taken simultaneously with radar observations suggests that the proportional coefficient relating the Thorpe scale and Ozmidov scale (see equation (1)) is not constant in the free atmosphere. This point was discussed in previous studies using oceanic microstructure observations and DNS, which showed that the coefficient is dependent on the depth of overturning layers and source of turbulence (Fritts et al., 2016; Mater et al., 2015; Scotti, 2015). Thus, it seems to be difficult to determine an appropriate proportional coefficient, which may be a weak function of some nondimensional numbers. Nevertheless, the Thorpe analysis seems promising for deriving turbulent parameters since the radiosonde-based estimates showed a similar variation in the height and seasonal variation of the ε to the radar-based estimates. The examination of the proportional coefficient based on both DNS and observations is necessary for a comprehensive validation of the Thorpe analysis in the free atmosphere.

At Syowa Station, the PANSY radar continues taking observations and the twice-daily radiosonde measurements are available. Thus, more than 700 simultaneous observations from the radar and radiosondes are obtained every year, although about half of the radiosonde observations are performed in the daytime. The large number of data will provide the local time dependence, climatology, and interannual variability of turbulent parameters in the Antarctic and, at the same time, enable us to explore the dependence of the proportional coefficient on the background field statistically.

Last, the present study used nighttime radiosonde measurements only because the daytime raw temperature profiles contained large errors from noise, which are clearly observed in the altitudes higher than 10 km (Figure 1). This point is also discussed in the recently published paper (Wilson et al., 2018). The noise characteristics including the amplitude and frequency depend on their cause: for example, spikes due to the balloon wake depend on the package shape and the length of the suspension line as well as the response time of the sensor (Shimizu & Hasebe, 2010). Thus, Thorpe analysis based on daytime radiosonde observations should be interpreted with caution.

Acknowledgments

This study is supported by JSPS KAKENHI grant JP16K17801 and JST CREST grant JPMJCR1663. PANSY is a multi-institutional project with core members from The University of Tokyo, the National Institute of Polar Research, and the Kyoto University. The PANSY radar and radiosonde measurements at Syowa Station are operated by the Japanese Antarctic Research Expedition (JARE). The PANSY radar observational data are available at the project website, http://pansy.eps.s.u-tokyo.ac.jp. Radiosonde observation data at Syowa Station are provided by the JMA. The time of sunset and sunrise at Syowa Station are provided by the National Astronomy Observatory of Japan's website (http://eco.mtk.nao.ac.jp/cgi-bin/koyomi/koyomix_en.cgi). All graphics were drawn by software developed by the Dennou-Ruby Davis project. We appreciate Takashi Ijichi's valuable comments on the Thorpe analysis and oceanic turbulence in the early stage of the present study. We also thank Takuji Sugidachi at Meisei Electric Corporation for instructive comments on the radiosondes that the present study used. Finally, we acknowledge L. Kantha, R. Wilson, and one anonymous reviewer for greatly helping us to improve this manuscript.

References

Alisse, J.-R., & Sidi, C. (2000). Experimental probability density functions of small-scale fluctuations in the stably stratified atmosphere. *Journal of Fluid Mechanics*, *402*, 137–162. https://doi.org/10.1017/S0022112099006813

Batchelor, G. K. (1953). *The theory of homogeneous turbulence*. Cambridge: Cambridge University Press.

Becker, E. (2012). Dynamical control of the middle atmosphere. *Space Science Reviews*, *168*(1–4), 283–314. https://doi.org/10.1007/s11214-011-9841-5

Bellenger, H., Wilson, R., Davison, J. L., Duvel, J. P., Xu, W., Lott, F., & Katsumata, M. (2017). Tropospheric turbulence over the tropical open ocean: Role of gravity waves. *Journal of the Atmospheric Sciences*, *74*(4), 1249–1271. https://doi.org/10.1175/Jas-D-16-0135.1

Birner, T. (2006). Fine-scale structure of the extratropical tropopause region. *Journal of Geophysical Research*, *111*, D04104. https://doi.org/10.1029/2005JD006301

Clayson, C. A., & Kantha, L. (2008). On turbulence and mixing in the free atmosphere inferred from high-resolution soundings. *Journal of Atmospheric and Oceanic Technology*, *25*(6), 833–852. https://doi.org/10.1175/2007jtecha992.1

Dehghan, A., & Hocking, W. K. (2011). Instrumental errors in spectral-width turbulence measurements by radars. *Journal of Atmospheric and Solar-Terrestrial Physics*, *73*(9), 1052–1068. https://doi.org/10.1016/j.jastp.2010.11.011

Delage, D., Roca, R., Bertin, F., Delcourt, J., Cremieu, A., Massebeuf, M., et al. (1997). A consistency check of three radar methods for monitoring eddy diffusion and energy dissipation rates through the tropopause. *Radio Science*, *32*(2), 757–767. https://doi.org/10.1029/96RS03543

Dietmüller, S., Eichinger, R., Garny, H., Birner, T., Boenisch, H., Pitari, G., et al. (2018). Quantifying the effect of mixing on the mean age of air in CCMVal-2 and CCMI-1 models. *Atmospheric Chemistry and Physics*, *18*(9), 6699–6720. https://doi.org/10.5194/acp-18-6699-2018

Dietmüller, S., Garny, H., Ploger, F., Jockel, P., & Cai, D. (2017). Effects of mixing on resolved and unresolved scales on stratospheric age of air. *Atmospheric Chemistry and Physics*, *17*(12), 7703–7719. https://doi.org/10.5194/acp-17-7703-2017

Dillon, T. M. (1982). Vertical overturns—A comparison of Thorpe and Ozmidov length scales. *Journal of Geophysical Research*, *87*(C12), 9601–9613. https://doi.org/10.1029/JC087iC12p09601

Dirksen, R. J., Sommer, M., Immler, F. J., Hurst, D. F., Kivi, R., & Vomel, H. (2014). Reference quality upper-air measurements: GRUAN data processing for the Vaisala RS92 radiosonde. *Atmospheric Measurement Techniques*, *7*(12), 4463–4490. https://doi.org/10.5194/amt-7-4463-2014

Dole, J., Wilson, R., Dalaudier, E., & Sidi, C. (2001). Energetics of small scale turbulence in the lower stratosphere from high resolution radar measurements. *Annales de Geophysique*, *19*(8), 945–952. https://doi.org/10.5194/angeo-19-945-2001

Frehlich, R., & Sharman, R. (2010). Climatology of velocity and temperature turbulence statistics determined from rawinsonde and ACARS/AMDAR data. *Journal of Applied Meteorology and Climatology*, *49*(6), 1149–1169. https://doi.org/10.1175/2010jamc2196.1

Fritts, D. C., Wang, L., Geller, M. A., Lawrence, D. A., Werne, J., & Balsley, B. B. (2016). Numerical modeling of multiscale dynamics at a high Reynolds number: Instabilities, turbulence, and an assessment of Ozmidov and Thorpe scales. *Journal of the Atmospheric Sciences*, *73*(2), 555–578. https://doi.org/10.1175/Jas-D-14-0343.1

Fukao, S., Hamazu, K., & Doviak, R. J. (2014). *Radar for meteorological and atmospheric observations*. Springer.
Fukao, S., Yamanaka, M. D., Ao, N., Hocking, W. K., Sato, T., Yamamoto, M., et al. (1994). Seasonal variability of vertical eddy diffusivity in the middle atmosphere: 1. Three-year observations by the middle and upper atmosphere radar. *Journal of Geophysical Research*, *99*(D9), 18,973–18,987. https://doi.org/10.1029/94JD00911
Gavrilov, N. M., Luce, H., Crochet, M., Dalaudier, F., & Fukao, S. (2005). Turbulence parameter estimations from high-resolution balloon temperature measurements of the MUTSI-2000 campaign. *Annales de Geophysique*, *23*(7), 2401–2413. https://doi.org/10.5194/angeo-23-2401-2005
Hocking, W. K. (1983). On the extraction of atmospheric turbulence parameters from radar backscatter Doppler spectra—I. Theory. *Journal of Atmospheric and Terrestrial Physics*, *45*(2–3), 89–102. https://doi.org/10.1016/S0021-9169(83)80013-0
Hocking, W. K. (1985). Measurement of turbulent energy-dissipation rates in the middle atmosphere by radar techniques—A review. *Radio Science*, *20*(6), 1403–1422. https://doi.org/10.1029/RS020i006p01403
Hocking, W. K. (1988). 2 years of continuous measurements of turbulence parameters in the upper mesosphere and lower thermosphere made with a 2-Mhz radar. *Journal of Geophysical Research*, *93*(D3), 2475–2491. https://doi.org/10.1029/JD093iD03p02475
Hocking, W. K. (1996). An assessment of the capabilities and limitations of radars in measurements of upper atmosphere turbulence. *Advances in Space Research*, *17*(11), 37–47. https://doi.org/10.1016/0273-1177(95)00728-W
Hocking, W. K. (1999). The dynamical parameters of turbulence theory as they apply to middle atmosphere studies. *Earth, Planets and Space*, *51*(7–8), 525–541. https://doi.org/10.1186/Bf03353213
Hocking, W. K. (2011). A review of mesosphere-stratosphere-troposphere (MST) radar developments and studies, circa 1997–2008. *Journal of Atmospheric and Solar-Terrestrial Physics*, *73*(9), 848–882. https://doi.org/10.1016/j.jastp.2010.12.009
Hocking, W. K., Röttger, J., Palmer, R. D., Sato, T., & Chilson, P. B. (2016). *Atmospheric radar: Application and science of MST radars in the Earth's mesosphere, stratosphere, troposphere, and weakly ionized regions*. Cambridge: Cambridge University Press. https://doi.org/10.1017/9781316556115
Hoskins, B. J., McIntyre, M. E., & Robertson, A. W. (1985). On the use and significance of isentropic potential vorticity maps. *Quarterly Journal of the Royal Meteorological Society*, *111*(470), 877–946. https://doi.org/10.1256/Smsqj.47001
Huang, N. E., & Wu, Z. H. (2008). A review on Hilbert-Huang transform: Method and its applications to geophysical studies. *Reviews of Geophysics*, *46*, RG2006. https://doi.org/10.1029/2007RG000228
Kantha, L., & Hocking, W. (2011). Dissipation rates of turbulence kinetic energy in the free atmosphere: MST radar and radiosondes. *Journal of Atmospheric and Solar-Terrestrial Physics*, *73*(9), 1043–1051. https://doi.org/10.1016/j.jastp.2010.11.024
Kantha, L., Lawrence, D., Luce, H., Hashiguchi, H., Tsuda, T., Wilson, R., et al. (2017). Shigaraki UAV-Radar Experiment (ShUREX): Overview of the campaign with some preliminary results. *Progress in Earth and Planetary Science*, *4*(1). https://doi.org/10.1186/s40645-017-0133-x
Kantha, L., & Luce, H. (2018). Mixing coefficient in stably stratified flows. *Journal of Physical Oceanography*, *48*(11), 2649–2665. https://doi.org/10.1175/JPO-D-18-0139.1
Kizu, N., Sugidachi, T., Kobayashi, E., Hoshino, S., Shimizu, K., Maeda, R., & Fujiwara, M. (2018). Technical characteristics and GRUAN data processing for the Meisei RS-11G and iMS-100 radiosondes, *GRUAN-TD-5* (152 pp.).
Kobayashi, S., Ota, Y., Harada, Y., Ebita, A., Moriya, M., Onoda, H., et al. (2015). The JRA-55 reanalysis: General specifications and basic characteristics. *Journal of the Meteorological Society of Japan*, *93*(1), 5–48. https://doi.org/10.2151/jmsj.2015-001
Labitt, M. (1979). Some basic relations concerning the radar measurement of air turbulence, Mass. Inst. of Technol., Lincoln Lab., Work. Pap. 46WP-5001.
Li, Q., Rapp, M., Schron, A., Schneider, A., & Stober, G. (2016). Derivation of turbulent energy dissipation rate with the Middle Atmosphere Alomar Radar System (MAARSY) and radiosondes at Andoya, Norway. *Annales de Geophysique*, *34*(12), 1209–1229. https://doi.org/10.5194/angeo-34-1209-2016
Love, P. T., & Geller, M. A. (2012). Research using high (and higher) resolution radiosonde data. *Eos, Transactions American Geophysical Union*, *93*(35), 337–338. https://doi.org/10.1029/2012EO350001
Luce, H., Fukao, S., Dalaudier, F., & Crochet, M. (2002). Strong mixing events observed near the tropopause with the MU radar and high-resolution balloon techniques. *Journal of the Atmospheric Sciences*, *59*(20), 2885–2896. https://doi.org/10.1175/1520-0469(2002)059<2885:Smeont>2.0.Co;2
Luce, H., Wilson, R., Dalaudier, F., Hashiguchi, H., Nishi, N., Shibagaki, Y., & Nakajo, T. (2014). Simultaneous observations of tropospheric turbulence from radiosondes using Thorpe analysis and the VHF MU radar. *Radio Science*, *49*, 1106–1123. https://doi.org/10.1002/2013rs005355
Mater, B. D., Venayagamoorthy, S. K., Laurent, L. S., & Moum, J. N. (2015). Biases in Thorpe-scale estimates of turbulence dissipation. Part I: Assessments from large-scale overturns in oceanographic data. *Journal of Physical Oceanography*, *45*(10), 2497–2521. https://doi.org/10.1175/Jpo-D-14-0128.1
McIntyre, M. E. (1989). On dynamics and transport near the polar mesopause in summer. *Journal of Geophysical Research*, *94*(D12), 14,617–14,628. https://doi.org/10.1029/JD094iD12p14617
Minamihara, Y., Sato, K., Kohma, M., & Tsutsumi, M. (2016). Characteristics of vertical wind fluctuations in the lower troposphere at Syowa Station in the Antarctic revealed by the PANSY radar. *Solaiat*, *12*(0), 116–120. https://doi.org/10.2151/sola.2016-026
Nastrom, G. D., & Eaton, F. D. (1997). Turbulence eddy dissipation rates from radar observations at 5–20 km at White Sands Missile Range, New Mexico. *Journal of Geophysical Research*, *102*(D16), 19,495–19,505. https://doi.org/10.1029/97JD01262
Nastrom, G. D., & Eaton, F. D. (2005). Seasonal variability of turbulence parameters at 2 to 21 km from MST radar measurements at Vandenberg Air Force Base, California. *Journal of Geophysical Research*, *110*, D19110. https://doi.org/10.1029/2005JD005782
Ploeger, F., Riese, M., Haenel, F., Konopka, P., Muller, R., & Stiller, G. (2015). Variability of stratospheric mean age of air and of the local effects of residual circulation and eddy mixing. *Journal of Geophysical Research: Atmospheres*, *120*, 716–733. https://doi.org/10.1002/2014jd022468
Randel, W. J., Wu, F., & Forster, P. (2007). The extratropical tropopause inversion layer: Global observations with GPS data, and a radiative forcing mechanism. *Journal of the Atmospheric Sciences*, *64*(12), 4489–4496. https://doi.org/10.1175/2007jas2412.1
Rao, D. N., Ratnam, M. V., Rao, T. N., & Rao, S. V. B. (2001). Seasonal variation of vertical eddy diffusivity in the troposphere, lower stratosphere and mesosphere over a tropical station. *Annales de Geophysique*, *19*(8), 975–984. https://doi.org/10.5194/angeo-19-975-2001
Sato, K., Hashiguchi, H., & Fukao, S. (1995). Gravity waves and turbulence associated with cumulus convection observed with the UHF/VHF clear-air Doppler radars. *Journal of Geophysical Research*, *100*(D4), 7111–7119. https://doi.org/10.1029/95JD00198
Sato, K., Tsutsumi, M., Sato, T., Nakamura, T., Saito, A., Tomikawa, Y., et al. (2014). Program of the Antarctic Syowa MST/IS radar (PANSY). *Journal of Atmospheric and Solar-Terrestrial Physics*, *118*, 2–15. https://doi.org/10.1016/j.jastp.2013.08.022

Sato, T., & Woodman, R. F. (1982). Fine altitude resolution observations of stratospheric turbulent layers by the Arecibo 430 MHz radar. *Journal of the Atmospheric Sciences*, *39*(11), 2546–2552. https://doi.org/10.1175/1520-0469(1982)039<2546:FAROOS>2.0.CO;2

Schneider, A., Gerding, M., & Lubken, F. J. (2015). Comparing turbulent parameters obtained from LITOS and radiosonde measurements. *Atmospheric Chemistry and Physics*, *15*(4), 2159–2166. https://doi.org/10.5194/acp-15-2159-2015

Scotti, A. (2015). Biases in Thorpe-scale estimates of turbulence dissipation. Part II: Energetics arguments and turbulence simulations. *Journal of Physical Oceanography*, *45*(10), 2522–2543. https://doi.org/10.1175/Jpo-D-14-0092.1

Scotti, A., & White, B. (2014). Diagnosing mixing in stratified turbulent flows with a locally defined available potential energy. *Journal of Fluid Mechanics*, *740*, 114–135. https://doi.org/10.1017/jfm.2013.643

Shimizu, K., & Hasebe, F. (2010). Fast-response high-resolution temperature sonde aimed at contamination-free profile observations. *Atmospheric Measurement Techniques*, *3*(6), 1673–1681. https://doi.org/10.5194/amt-3-1673-2010

Smyth, W. D., Moum, J. N., & Caldwell, D. R. (2001). The efficiency of mixing in turbulent patches: Inferences from direct simulations and microstructure observations. *Journal of Physical Oceanography*, *31*(8), 1969–1992. https://doi.org/10.1175/1520-0485(2001)031<1969:Teomit>2.0.Co;2

Thorpe, S. A. (1977). Turbulence and mixing in a Scottish loch. *Philosophical Transactions of the Royal Society A: Mathematical, Physical and Engineering Sciences*, *286*(1334), 125–181. https://doi.org/10.1098/rsta.1977.0112

Tomikawa, Y., Nishimura, Y., & Yamanouchi, T. (2009). Characteristics of tropopause and tropopause inversion layer in the polar region. *SOLA*, *5*, 141–144. https://doi.org/10.2151/sola.2009-036

Tsuda, T., Sato, T., Hirose, K., Fukao, S., & Kato, S. (1986). MU radar observations of the aspect sensitivity of backscattered VHF echo power in the troposphere and lower stratosphere. *Radio Science*, *21*(6), 971–980. https://doi.org/10.1029/RS021i006p00971

Weinstock, J. (1981). Using radar to estimate dissipation rates in thin-layers of turbulence. *Radio Science*, *16*(6), 1401–1406. https://doi.org/10.1029/RS016i006p01401

White, A. B., Lataitis, R. J., & Lawrence, R. S. (1999). Space and time filtering of remotely sensed velocity turbulence. *Journal of Atmospheric and Oceanic Technology*, *16*(12), 1967–1972. https://doi.org/10.1175/1520-0426(1999)016<1967:Satfor>2.0.Co;2

Wilson, R. (2004). Turbulent diffusivity in the free atmosphere inferred from MST radar measurements: A review. *Annales de Geophysique*, *22*(11), 3869–3887. https://doi.org/10.5194/angeo-22-3869-2004

Wilson, R., Dalaudier, F., & Luce, H. (2011). Can one detect small-scale turbulence from standard meteorological radiosondes? *Atmospheric Measurement Techniques*, *4*(5), 795–804. https://doi.org/10.5194/amt-4-795-2011

Wilson, R., Hashiguchi, H., & Yabuki, M. (2018). Vertical spectra of temperature in the free troposphere at meso-and-small scales according to the flow regime: Observations and interpretation. *Atmosphere*, *9*(11), 415. https://doi.org/10.3390/atmos9110415

Wilson, R., Luce, H., Dalaudier, F., & Lefrere, J. (2010). Turbulence patch identification in potential density or temperature profiles. *Journal of Atmospheric and Oceanic Technology*, *27*(6), 977–993. https://doi.org/10.1175/2010jtecha1357.1

Wilson, R., Luce, H., Hashiguchi, H., Nishi, N., & Yabuki, Y. (2014). Energetics of persistent turbulent layers underneath mid-level clouds estimated from concurrent radar and radiosonde data. *Journal of Atmospheric and Solar-Terrestrial Physics*, *118*, 78–89. https://doi.org/10.1016/j.jastp.2014.01.005

Wilson, R., Luce, H., Hashiguchi, H., Shiotani, M., & Dalaudier, F. (2013). On the effect of moisture on the detection of tropospheric turbulence from in situ measurements. *Atmospheric Measurement Techniques*, *6*(3), 697–702. https://doi.org/10.5194/amt-6-697-2013

Yoshiki, M., Kizu, N., & Sato, K. (2004). Energy enhancements of gravity waves in the Antarctic lower stratosphere associated with variations in the polar vortex and tropospheric disturbances. *Journal of Geophysical Research*, *109*, D23104. https://doi.org/10.1029/2004JD004870

Yoshiki, M., & Sato, K. (2000). A statistical study of gravity waves in the polar regions based on operational radiosonde data. *Journal of Geophysical Research*, *105*(D14), 17,995–18,011. https://doi.org/10.1029/2000JD900204